Phase-controllable large-area two-dimensional In_2Se_3 and ferroelectric hetero-phase junction

Wei Han[1,2,+], Xiaodong Zheng[1,2,+], Ke Yang[1,3,+], Chi Shing Tsang[1], Fangyuan Zheng[1,2], Lok Wing Wong[1,2], Ka Hei Lai[1], Tiefeng Yang[4,5], Qi Wei[1], Mingjie Li[1], Weng Fu Io[1], Feng Guo[1], Yuan Cai[6], Ning Wang[6], Jianhua Hao[1], Shu Ping Lau[1], Chun-Sing Lee[4], Thuc Hue Ly[4,5,*], Ming Yang[1,2*], and Jiong Zhao[1,2,*]

[1]Department of Applied Physics, The Hong Kong Polytechnic University, Kowloon, Hong Kong, China

[2]The Hong Kong Polytechnic University Shenzhen Research Institute, Shenzhen, China

[3]Department of Computing, The Hong Kong Polytechnic University, Kowloon, Hong Kong, China

[4]Department of Chemistry and Center of Super-Diamond & Advanced Films (COSDAF), City University of Hong Kong, Kowloon, Hong Kong, China

[5]City University of Hong Kong Shenzhen Research Institute, Shenzhen, China

[6]Department of Physics, Hong Kong University of Science and Technology, Hong Kong, China

[*]E-mail: jiongzhao@polyu.edu.hk

kevin.m.yang@polyu.edu.hk

thuchly@cityu.edu.hk

[+]These authors contribute equally to this work.

Abstract

Memory transistors based on two-dimensional (2D) ferroelectric semiconductors are intriguing for next-generation in-memory computing, which may surpass the prevailing Von Neumann architecture. To date several 2D FE materials have been unveiled, among which 2D In_2Se_3 is the most promising, as all the paraelectric (PE) (β), ferroelectric (FE) (α) and antiferroelectric (AFE) (β′) phases can be attained in the 2D quintuple layers. However, the large-scale synthesis of 2D In_2Se_3 film with desired phase is still in absence, and the stability conditions for each phase remain obscure. Here, we show the successful growth of centimetre (cm)-scale 2D β-In_2Se_3 film by chemical vapor deposition (CVD). We also obtain distinct cm-scale 2D β′-In_2Se_3 film by InSe precursor addition during CVD. More importantly, we demonstrate that as-grown 2D β′-In_2Se_3 film on mica substrates can be delaminated or transferred onto flexible or uneven substrates which simultaneously yields cm-scale 2D α-In_2Se_3 film through complete phase transition. Thus, a full spectrum of PE, FE and AFE 2D films are readily obtained by means of the correlated polymorphism in 2D In_2Se_3, enabling 2D memory transistors with high electron mobility (29 and 53 $cm^2\ V^{-1}s^{-1}$ in reverse sweep for β′- and α-In_2Se_3, respectively), and polarizable β′-α In_2Se_3 hetero-phase junctions with improved non-volatile memory performance. Our work pioneers in tailoring the 2D FE structures by precise phase engineering, and unlocks their great potentials for logic-in-memory electronics.

Introduction

Two-dimensional (2D) ferroelectric (FE) semiconductors with switchable polarization provide a versatile platform for novel applications, such as ferroelectric field-effect transistor (FE-FET or memory transistor), [1,2] nonvolatile memory (NVM), [3,4] in-memory sensor, [5] and neuromorphic computing. [3] Compared with the conventional von Neumann systems, [6] 2D FE-FET integrates the logic operation and memory storage functions, having potential to miniaturize the devices and reduce the energy consumption in future. [7-9] So far, among the reported 2D FE semiconductors (e.g., In_2Se_3, [10-13] SnTe, [14] $CuInP_2S_6$, [15] $MoTe_2$, [16] and SnS [17]), α-In_2Se_3 possesses a markedly outstanding carrier mobility. [1] Besides, it has appropriate band gap (~1.39 eV) as well as room-temperature out-of-plane and in-plane ferroelectricity down to monolayer limit [11-13]. 2D In_2Se_3 is also attractive for its polymorphism, in which the energy difference among β-In_2Se_3, β′-In_2Se_3 and α-In_2Se_3 is small, thereby facilitating the transitions among these three phases. Particularly, β′-In_2Se_3 has room-temperature in-plane ferroelectricity [18] or antiferroelectric (AFE) structures, [19-21] ferroelasticity, [22] and high carrier mobility by theoretical calculation.[23] The correlated polymorphism and ferroelectricity in 2D In_2Se_3 provide vast opportunities in tailoring the FE structures and properties, making 2D In_2Se_3 a suitable candidate for memory transistor and other emergent applications.

Despite the appealing application potentials, large-area synthesis of 2D In_2Se_3 film, which is essential for large-scale integration, is still challenging. Besides, the complicated polymorphism (α, β, β′, and γ) [24] and low phase-transition temperatures between the In_2Se_3 phases (β′→β at around 250 °C, α→β at around 270 °C) [13,25] usually lead to the coexistence of multi-phases during the growth, [13,26] inaccessible to pure-phase In_2Se_3 films. Although the high-temperature β-phase nanosheets have been synthesized by chemical vapor deposition (CVD), their size is still limited to a few hundred micrometers. [27,28] As a metastable phase of β, the superstructures of β′ have been observed as early as 1975, [29] yet so far, pure phase β′ films cannot be synthesized directly by CVD, found only in the mixed phase. [13,30] By now, only a few groups were able to obtain α-phase 2D In_2Se_3 flakes by CVD growth, but their lateral sizes were limited to ~100 μm, [11,31] far below the requirement of large-scale integration. [32] Furthermore, semiconducting hetero- or homo-junctions in electronic and

optoelectronic devices plays critical roles, but they were previously overlooked in 2D FE materials and devices. The interfaces between distinct phases with varied polarizations can give rise to novel properties that do not exist in the counterpart single phases.

Therefore, in this study, we aim in (1) precise phase control in 2D In_2Se_3, (2) large-area growth of 2D In_2Se_3, and (3) fabrication of hetero-phase junction. The first target relies on in-depth understanding in the stability for each phase of 2D In_2Se_3, especially under the influences of defects and strains, which prevalently exist in chemical vapor deposition (CVD) products. The second target requests to overcome the difficulties in controlling the concentrations of precursors owing to long-distance source-to-substrate transport (>10 cm) by traditional CVD. [33] The third target depends on the achievement of the phase control (first target).

Herein, we present a CVD method to grow large-area 2D In_2Se_3 films (see the schematic diagram in **Supplementary Fig. 1**). Benefited from the ultra-short transport distances for precursors (1~3 mm), a stable source supply leads to continuous growth of cm-scale 2D β-In_2Se_3 films. After that, by intendedly introducing InSe powder in the source, we obtain large-area β′-In_2Se_3 films. Finally, we transfer large-area β′-In_2Se_3 films to flexible substrates and successfully achieve large-area α-In_2Se_3 films. Our experimental and theoretical mechanistic studies confirm the seeding effect of InSe crystals which triggers the transition from β to β′ phase, and the mechanical strain is responsible for the β′-to-α phase transition. Memory transistor devices are constructed using the as-prepared large-area 2D films, and all the three phases exhibit remarkable field-effect regulation performances. The β′- and α-In_2Se_3 memory devices with large hysteresis windows upon electric gating control exhibit long retention time and robust cycle endurance. At last, we successfully prepare the β′-α hetero-phase junctions, which show even wider gating hysteresis windows and substantially improved non-volatile memory properties.

Results and discussion

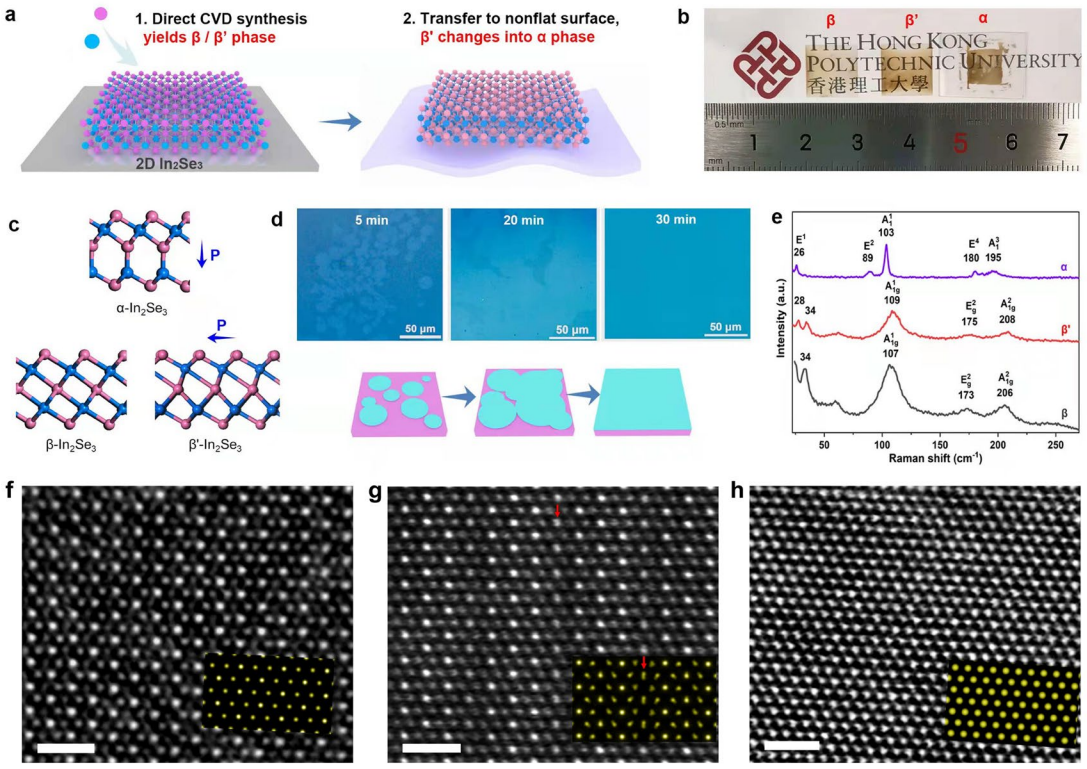

Fig. 1 Phase-controlled synthesis of large-area 2D In_2Se_3 films. a, Schematic diagrams of the controlled synthesis of β-, β′-, and α- In_2Se_3 films. The β and β′ phases were directly grown by CVD and the α phase was obtained by phase transition after transferring β′ to non-flat surfaces. Peak balls represent gaseous Se precursor, and blue balls represent gaseous indium-containing precursor ($In_2O_{3-x}Se_x$ and/or $InSe_{1+y}$). **b**, Photo of the obtained large-area In_2Se_3 films of three phases (β and β′ on mica, α on PET). **c**, The side-view crystal models simulated by DFT calculations on α-, β-, and β′-In_2Se_3. Red balls represent Se atoms, and blue balls represent In atoms. The blue arrows highlight the main polarization directions. **d**, Growth-time-dependent optical images of β-In_2Se_3 films at 5, 20, and 30 min (up panels). Schematic diagram of the growth mechanism of continuous β-In_2Se_3 films (down panels). It includes three stages: (i) nucleation (ii) growing (iii) merging and stitching. **e**, Raman spectra of the 2D In_2Se_3 films of the three phases. **f-h**, The atomic ADF-STEM images of the β, β′ and α- In_2Se_3. Insets show the simulated ADF-STEM images of corresponding phases. Scalebars, 1 nm.

Large-area cm-scale synthesis of three phases (β, distorted β (β′), and α) of In_2Se_3 films is achieved by using CVD and phase-transition transfer (PTT) methods (see Methods), as depicted in **Fig. 1a, b** and **Supplementary Fig. 1**. For bulks, all the three phases

have rhombohedral structures with space groups of *R-3m* (166) for β/β′ phase and *R3m* (160) for α phase. The atomic structures (side-view) of α-, β-, and β′- In_2Se_3 are shown in **Fig. 1c** (only one layer is shown). Similar Se-In-Se-In-Se quintuple layers can be seen with different sites or displacements of the central Se layer. The shifting of Se atoms in the central layer creates out-of-plane (major) and in-plane (minor) ferroelectricity in α phase, [10] and in-plane polarization in β′ phase. [18] In particular, the in-plane polarization in β′-In_2Se_3 can trigger the formation of 1D superstructures, in analogous to the antiferroelectric (AFE) stripe-like domains. [19]

Regarding the CVD growth of large-area 2D β-In_2Se_3 films, the precursors of In_2O_3 and Se powder, and the carrier gas of 5% H_2/N_2 are applied. Unlike traditional CVD setups (**Supplementary Fig. 2a** and **Supplementary Table 1**), [13] one of our solid precursors is placed directly below the growth substrate, and it is evaporated and deposited vertically upward onto the substrate (**Supplementary Fig. 2b**). Benefited from the ultra-short transport distances from precursors to substates (1~3 mm) in the CVD, [33] a stable and uniform precursors supply can lead to the continuous growth of cm-scale 2D In_2Se_3 films. Compared with the long-distance cases with growing small-size flakes, the short distance between the precursor and substrate (*ca.* 2 mm) significantly speeds up the growth and enlarges the final 2D flake size (**Supplementary Fig. 3 and Supplementary Table 1**). Thus, we successfully prepare cm-size 2D β-In_2Se_3 films on mica substrates (**Fig. 1b**). Briefly, in CVD chamber atmosphere, the gaseous indium-containing species react with Se, rendering 2D In_2Se_3 continuous films. [34] The time-dependent optical images of β-In_2Se_3 films at 5, 20, and 30 min, and the corresponding schematic diagrams demonstrate the three growth stages: (i) nucleation of small 2D β-In_2Se_3 crystals; (ii) growing up and merging; (iii) completely stitching and formation of continuous 2D β-In_2Se_3 films (**Fig. 1d**). The detailed growth chemistry and mechanisms for continuous β-In_2Se_3 film are discussed in **Supplementary Fig. 4, 5**. The thickness of the β-In_2Se_3 films is determined by atomic force microscopy (AFM) and optical microscopy (OM), typically ranging from ten layers down to the monolayer limit (~0.9 nm) (**Supplementary Fig. 6**). From higher-mag TEM images of some growing flakes and films, the edges show regular and well-faceted shapes, as shown in **Supplementary Fig. 7**. The angles between the growing edges are mostly 60° or 120°, revealing the good crystallinity. Thus, the crystals are possible to grow and stitch into a continuous

film. Continuous 2D films can be grown at various temperatures of 600-720 ℃ (**Supplementary Fig. 8**) with good repeatability (**Supplementary Fig. 9**). The growth temperature is in coincidence with the reported phase stability of β-In_2Se_3, implying this high-temperature β phase (compared with α phase) [27,28] is well preserved even after cooling down to room temperature by our CVD growth. Yet, control experiments on other substrates fail to obtain 2D In_2Se_3 films (**Supplementary Fig. 10**). In our CVD experiments, mica offers an atomically flat substrate which is suitable for nucleation and lateral growth of 2D In_2Se_3 films. More importantly, it provides sufficient mechanical support and maintains the in-plane cooling strain in the 2D In_2Se_3 film and avoids further phase transition upon cooling which generates other phases. We will elaborate on this later.

Next, by introducing additional β-InSe powder (**Supplementary Fig. 11**) into the In_2O_3 source in CVD (see Methods), large-area 2D β′-In_2Se_3 films can be grown on mica (**Fig. 1a, b**). β-InSe plays the role of seeding in CVD process and promotes the nucleation of β′-In_2Se_3. The detailed mechanisms will be discussed in the following as well. The characteristic stripe-like domain structures in β′-In_2Se_3 can be clearly identified by polarized-light optical microscope (for sample on growth substrate) and bright/dark-field TEM (for sample transferred on to TEM grid) (**Supplementary Fig. 12 and 13**). The observed 1D stripes in OM/TEM images and the satellite spots in selected area electron diffraction (SAED) are originated from long-range ordered superstructures due to the local displacements of Se and In atoms. We use scanning transmission electron microscopy (STEM) to measure the layer thickness of β′-In_2Se_3 films, as shown in **Supplementary Fig. 14**, and the β′ phase is determined in down to four-layer-thick film by SAED.

The phases of the bi-layer and mono-layer samples are not straightforwardly determined by single TEM. As we will present, the in-plane strain preserved in the as-grown samples, normally caused by the cooling strain and unmatched thermal expansion coefficients between the 2D film and substrates, [35,36] can be released during transfer of the 2D films onto non-flat or uneven surfaces. Hence, we can obtain the large-area continuous 2D α-In_2Se_3 films by transferring the as grown 2D β′-In_2Se_3 films to flexible polyethylene terephthalate (PET) substrates (see Methods) (**Fig. 1a, b**). During the transfer process, the in-plane strain exerted on the β′-In_2Se_3 films by

underlying mica substrate is relaxed and β′-In_2Se_3 completely turns into α-In_2Se_3 after bending PET for several times. The wrinkles in α-In_2Se_3 films on PET indicate that the films are delaminated with interfacial strain release (**Supplementary Fig. 15**).

Cross-identification by Raman spectroscopy (**Fig. 1e**) confirms the pure phase synthesis of 2D In_2Se_3 by our approach. β and β′ phases have similar vibration peaks including A_{1g}^1, E_g^2, and A_{1g}^2, while α phase has distinct peaks (E^2, A_1^1, E^4, and A_1^3). [11,37] Therefore the β, β′ and α phases can be unambiguously distinguished from the TEM and Raman results. The precise phase control aside, high quality crystallinity and grain structures have been carefully examined by TEM (**Supplementary Fig. 16**). The close angles within a deviation of 2 degree in SAED patterns prove that the 2D β and β′ In_2Se_3 films obtained are single crystalline. Moreover, no obvious grain boundary found from the dark-field TEM images also reveal the single crystalline growth of β and β′ In_2Se_3 films (**Supplementary Fig. 17**). For α-In_2Se_3 films, the phase transition can generate more wrinkles, and the crystal lattice directions can be slightly changed by the wrinkles. We have carefully checked the wrinkle positions of α- In_2Se_3 by TEM and SAED. As shown in **Supplementary Fig. 18**, the SAED patterns reveal that the lattices on two sides of the wrinkle have 1.2 degree of rotation. Some wrinkles will cause a lattice rotation up to 4.6 degree. Because of the wrinkles formed after strain relaxation, the small degree misalign can exist in a continuous α-In_2Se_3 film. The prepared α-In_2Se_3 films with spontaneous wrinkles are confirmed as continuous films by additional SEM characterizations (**Supplementary Fig. 19**). The atomic-resolution STEM-annular dark-field (ADF) images of the three respective phases are shown in **Fig. 1 f-h,** revealing the atomic configurations, which are in agreement with the DFT calculated structures and the corresponding multislice STEM image simulation results (insets) (see Methods). It is also noted the 2H stacking order (**Fig. 1f, g**) is dominant for all the phases of synthesized 2D In_2Se_3, while the 3R stacking order (**Fig. 1h**) is less observed. The β′ phase has apparent periodic 1D nanostripes along $[11\bar{2}0]$ crystal direction, owing to the AFE structures. [19] Additionally, we have collected the cross-section HAADF-STEM images for multilayer α-In_2Se_3 and β-In_2Se_3 (**Supplementary Fig. 20**). From the sketch images of crystal structure, we are able to see the α-In_2Se_3 is ABCCA stacking (within the quintuple layer) while the β-In_2Se_3 is ABCAB stacking (within the

quintuple layer). Therefore, we can easily differentiate these two phases from cross-section STEM results.

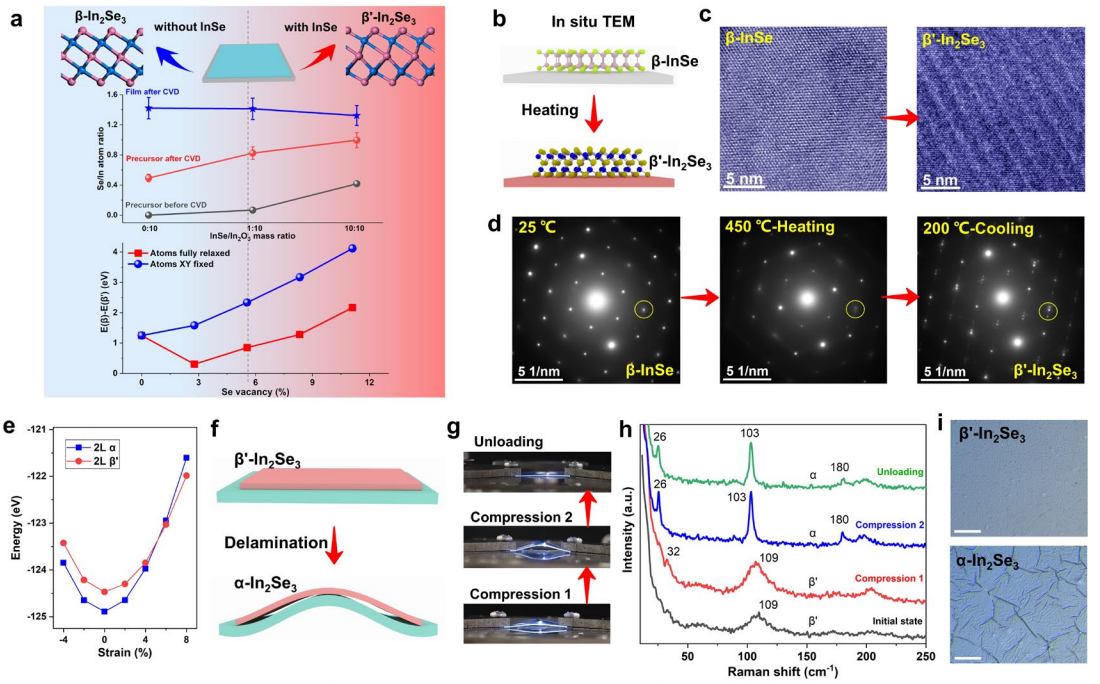

Fig. 2 Phase-control mechanisms of 2D In_2Se_3 films. a, The sketch map of phase-control strategy, the evolution of Se/In atom ratio in precursors and films, and the DFT calculated energy difference between monolayer β and β′ phase dependent on Se vacancy density. **b**, Sketch map of the *in situ* heating TEM showing the transition from β-InSe to β′-In_2Se_3. **c**, HRTEM images of InSe flakes before and after heating at room temperature. **d**, *In situ* SAED patterns of β-InSe flake at 25 ℃, 450 ℃ (heating), and 200 ℃ (cooling). **e**, The calculated strain-dependent total energy for bi-layer β′ and α-In_2Se_3 films. **f**, Sketch map of *in situ* Raman testing on PET by a strain stage illustrating the transition from β′-In_2Se_3 to α-In_2Se_3. **g**, (bottom to up) Serial photos of the straining device during the compression process. **h**, *In situ* Raman spectra of β′-In_2Se_3 films under different compression states corresponding to **g**. **i**, Optical images of In_2Se_3 films on PET before phase change and after phase change. Scalebars = 10 μm.

As we mentioned, we control the β/β′ phase mainly through the β-InSe powder in CVD precursors. As shown in **Supplementary Fig. 21**, without using InSe, only β-In_2Se_3 can be obtained. When adding InSe into the precursor, regardless of the InSe:In_2O_3 ratio (1:10 and 10:10), we can acquire β′-In_2Se_3 films. If using pure InSe powders without

any In_2O_3 in the precursor, the obtained small-size In_2Se_3 crystals are still in β′ phase (**Supplementary Fig. 22**), obeying this simple but robust concept for preparing 2D β and β′-In_2Se_3. For studying the phase-control mechanism, we investigated the change of Se/In ratio in different growth batches by studying the EDS spectra in precursors and In_2Se_3 films, as shown in **Fig. 2a**. The EDS results are averaged over multiple points for each sample with an error ~ 10%, and qualitatively show the sample compositions. Before CVD, the Se/In ratios in precursors are 0, 0.07, and 0.42 as controlled by the mass ratio of InSe/In_2O_3 (Se power is not counted here). After CVD, the Se/In ratios in precursors are 0.49, 0.82, and 0.99 correspondingly. We find that an addition of 6.7% Se ratio before CVD leads to a significant increase (33%) in Se proportion after CVD. In the products, we observed the Se/In ratio in In_2Se_3 films is slightly reduced by varying the precursors. The Se/In ratio of In_2Se_3 films in different growth batches change from 1.42 to 1.41, and then to 1.32 (**Supplementary Fig. 23**). It shows that the Se/In ratio in products is indeed controlled by the InSe/ In_2O_3 ratio, and the Se vacancy increases in films with increasing the Se/In ratio in precursors. Therefore, the Se/In ratio is critical to tune the β/β′ phases of In_2Se_3. The seeding effect of InSe also cannot be overlooked, as shown in **Supplementary Fig. 24**, prior to heating, the original precursors in boat are In_2O_3 and InSe mixed powders. During heating, the precursors in boat turn to intermediate products $In_2O_{3-x}Se_x$ and $InSe_{1+y}$. The $In_2O_{3-x}Se_x$ is confirmed by Raman in **Supplementary Fig. 4b**. The $InSe_{1+y}$ is confirmed by XRD and EDS after CVD in **Supplementary Fig. 25** and **Supplementary Fig. 22**. On mica, the gaseous $InSe_{1+y}$ reacts with Se to grow *β'*-In_2Se_3 seeds, which is confirmed by OM, Raman, TEM, and SAED experiments in an additional control experiment using pure InSe powder as precursor (no In_2O_3 is used, however, pure InSe precursor cannot yield large area thin film) (**Supplementary Fig. 22**). After seeds formation, the gaseous $In_2O_{3-x}Se_x$ and $InSe_{1+y}$ react with Se and H_2 to further grow *β'*-In_2Se_3 flakes. Finally, the *β'*-In_2Se_3 flakes are merged to form the continuous *β'*-In_2Se_3 films.

We also compare the ground state energies of monolayer β/β′ phases with different Se vacancy concentrations by DFT calculations, as shown in **Fig. 2a**. Upon all atoms fully relaxed, except for the low Se vacancy concentration state (0-3%), the energy differences between β phase and β′ phase monotonically increase with the increase of

Se vacancy in monolayer In_2Se_3 (3-12%), manifesting the enhanced stability of β′ phase as compared to β phase under Se-deficient conditions. The Se deficiency even can immediately turn the β-InSe crystal into β′-In_2Se_3 under high temperature. In order to make the physics clear, we also calculated the energy difference by fixing the atomic positions at X and Y direction. When Se vacancy introduced, the total energy difference keeps linear increasing, which further indicates that the stability of β′ phase increases with the Se vacancy concentration. Further, we conduct *in situ* TEM heating experiments (see Methods) on β-InSe flakes (**Fig. 2b**). As shown in **Fig. 2d**, when the β-InSe is heated up to 450 ℃, the SAED pattern starts to exhibit faint satellite spots, different from the initial state of β-InSe at room temperature. After cooling back to 200 ℃, the satellite spots become even sharper, showing the formation of β′-In_2Se_3 crystals. The HRTEM image during heating also shows the ordering structure of nanostripes as β′-In_2Se_3 (**Fig. 2c)**. Considering the more than 30% Se deficiency in the initial InSe crystal compared with In_2Se_3, the higher stability for the final β′-In_2Se_3 can be rationalized. We carry out non-destructive XPS measurement to confirm the existence of Se vacancies in the as-grown β′-In_2Se_3 films on mica, as shown in **Supplementary Fig. 26** and **Supplementary Table 2**. The mixed valence of In is in line with our analysis on the Se vacancy in β' phase. The In peak splitting is much less obvious in 0:10 and 1:10 samples, which can be attributed to less amount of vacancies in the samples. Regarding the XPS peak of Se, the peaks of Se 3p moved toward lower binding energy compared to the Se peaks in 0:10 and 1:10 samples, which affirms the presence of Se vacancies. For β-In_2Se_3 film, from the atomic STEM-HAADF images shown in **Supplementary Fig. 27**, we observe some atomic columns have significantly lower intensity compared with the defect-free image, revealing Se vacancies in β-In_2Se_3. Thus, we can attribute the successful β/β′ phase control in our CVD approach to the Se deficiency strategy.

Strain engineering for phase control arouses interests in 2D materials, like MoS_2,[38] and $MoTe_2$, [39] however no reports on 2D In_2Se_3 yet. We also employ DFT calculations to examine the energy evolutions under strain for β′ and α phases, in which the total energy in different layer thicknesses (1L, 2L, 4L, 6L, and bulk) has been calculated and shown in **Fig. 2e** and **Supplementary Fig. 28**. The in-equilibrium lattice constants for β′ and α phases are quite close, thus we can directly compare the strain in the following.

For bi-layer In_2Se_3, the energy of α phase is lower than that of β′ phase under a strain range of -4%~4%. Under a tensile strain above 6%, the energy of α phase becomes higher than β′ phase. Based on thermodynamics, the β′ phase can transform into α phase within the (tensile) strain range of *ca.* 3%-8%, or vice versa. Next we use *in situ* Raman spectroscopy to verify the strain induced phase transition mechanism (β′-In_2Se_3 to α-In_2Se_3) using samples on flexible PET substrate (**Fig. 2f,g**). We test the Raman spectra under different compression curvatures of PET. As illustrated in **Fig. 2h**, under the initial and compression 1 state, the In_2Se_3 film remains β′ phase. When loaded to compression 2 state with higher curvature, the In_2Se_3 film experiences a sudden phase change from β′ to α and maintain α phase even after unloading. This sudden and irreversible phase change and the apparent wrinkles in α-In_2Se_3 films reveal that the film delamination and interfacial strain release is the main cause of such phase transition (**Fig. 2i**). This concept can explain the spontaneous large-area α-In_2Se_3 formation after transferring the 2D β′-In_2Se_3 films from the original flat mica surface to uneven/non-flat, or even suspended substrates.

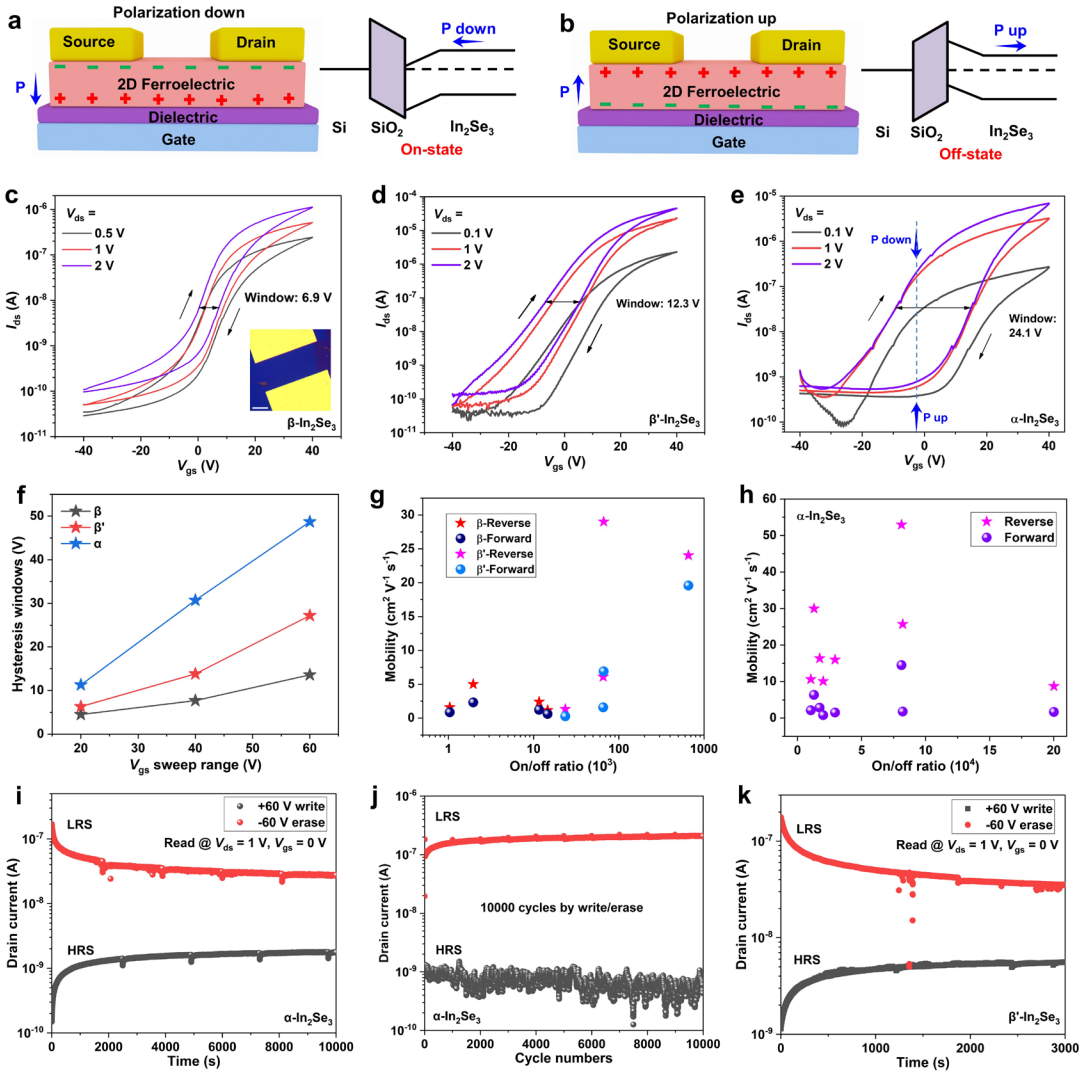

Fig. 3 Working mechanism and performances of ferroelectric field-effect transistors (FE-FET) based on 2D In_2Se_3 films. a, b, Schemes of FE-FET device (above) and the corresponding band diagrams (below) with polarization (P) down state (**a**) and P up state (**b**). **c-e**, The hysteresis transfer characteristic loops of β-, β′-, and α-In_2Se_3 devices during double sweeping with various V_{ds}. Inset in **c**: optical image of a typical In_2Se_3 FET device. Scalebar = 20 μm. **f**, The hysteresis windows plotted with various gate-voltage sweep ranges of β-, β′-, and α-In_2Se_3 devices. **g**, Field-effect mobility and on/off current ratio of various β and β′ In_2Se_3 devices. **h**, Mobility and on/off current ratio of various α-In_2Se_3 devices and other CVD-grown 2D films. **i**, Retention testing of α-In_2Se_3 NVM device by gate-voltage control. **j**, The robust endurance of α-In_2Se_3 device after 10000 write and erase cycles, without degradation of HRS and LRS. **k**, Retention measurement on β′-In_2Se_3 NVM device.

The out-of-plane ferroelectricity of α phase have been confirmed by piezoresponse force microscopy (PFM) measurements (**Supplementary Fig. 29**). Furthermore, the non-centrosymmetric crystal structure of α phase and centrosymmetric crystal structure of β' phase are verified by second harmonic generation (SHG) tests (**Supplementary Fig. 30, 31**). Then, the ferroelectric field-effect transistors (FE-FET) using these 2D semiconductors as the channel are designed and depicted in **Fig. 3a, b**. When the FE semiconductor is in polarization (P) down state, the mobile carriers (electrons for n-type In_2Se_3) redistributed by the FE dipole moment will bend the electron bands in the channel, especially at interfaces near dielectric layer. In other words, the downward polarization increases the carrier density in the FET channel (**Fig. 3a**). On the contrary, when the FE semiconductor is in P-up state, the channel carrier density can be reduced (**Fig. 3b**). Therefore, the switch of FE polarization using gate-voltage (V_{gs}) causes hysteresis effect, and memory window appears in the transfer curves. The FE-FET devices are operated alternatively between on and off-states by the gating control.

Here in the three phases of 2D In_2Se_3, β phase is paraelectric due to its centrosymmetric crystal structure, α phase has both in-plane and out-of-plane ferroelectricity,[13] and the β′ phase has anti-ferroelectricity. [18,19] We transfer these three types of 2D In_2Se_3 films to Si substrates with 300 nm SiO_2 layer for FET device fabrication and testing. All the devices are encapsulated and passivated by 10 nm-thick Al_2O_3 using atomic layer deposition (ALD) to avoid the attack from oxygen and moisture. As shown in **Fig. 3c**, the transfer characteristic loops of β-In_2Se_3 devices with various source-drain voltages (V_{ds}) reveal a small clockwise hysteresis window of about 6.9 V under -40 to 40 V sweeping. Since β-In_2Se_3 is non-ferroelectric, this small hysteresis may be caused by the charge trapping in the device. To verify this effect, we have changed the sweep rate of voltage to test the transfer characteristic loops (**Supplementary Fig. 32**). The hysteresis windows in β and β′ phase devices decrease with increasing sweep rate, but they do not vanish at a fast sweep rate. Hence, the hysteresis windows of β and β′ phases may come from the charge traps between the channel material and the substrate, or the intrinsic defects. In α devices, even with a fast sweep rate, there are still apparent hysteresis windows, which are associated with ferroelectricity.

The FETs made of our 2D β-In_2Se_3 possess high current on/off ratio (~10^4) as well as considerable mobility (~5 cm^2/Vs in reverse sweep) (**Fig. 3g**), better than that of recently reported CVD-grown β-In_2Se_3 films (1 cm^2/Vs). [40] On the other hand, the transfer characteristic loops of 2D β′-In_2Se_3 devices exhibit wider hysteresis windows of about 12.3 V, higher current on/off ratio (~6.6×10^5), and higher mobility (~29 cm^2/Vs in reverse sweep) (**Fig. 3d,g**). This performance is comparable with the widely studied CVD-grown 2D MoS_2 films (~30 cm^2/Vs) [41] and 2D $MoTe_2$ films (~45 cm^2/Vs). [42] Finally, as shown in **Fig. 3e** and **3h**, 2D α-In_2Se_3 devices have ultra-large hysteresis window of about 24.1 V, and high mobility up to 53 cm^2/Vs, with high current on/off ratio (~2×10^5), much higher than that of reported CVD-grown α-In_2Se_3 flakes (on/off ratio: 10^3, mobility: 2.5 cm^2/Vs). [43] Therefore, our 2D FE α-In_2Se_3 films are potential candidates for high-performance computing and memory devices, especially the logic-in-memory devices. The highest memory effect in 2D α-In_2Se_3 originates from its remarkable out-of-plane FE polarizations. The current output curves of three phases with various gate voltages are shown in **Supplementary Fig. 33**, which reveal that both β′- and α-In_2Se_3 devices can achieve large current over 20 μA under gate voltage of 40 V. The hysteresis windows plotted with gate-voltage sweep ranges of β-, β′-, and α-In_2Se_3 devices are shown in **Fig. 3f** and **Supplementary Fig. 34**.

Regarding the NVM performance, we have conducted the retention time and endurance measurements of α and β′ In_2Se_3 NVM devices, which show long retention time over 10000 s for α phase (3000 s for β′ phase) and remarkable cycle stability over 10000 write/erase cycles (7500 cycles for β′), as shown in **Fig. 3i-k** and **Supplementary Fig. 35**. A comprehensive performance comparison of our results with reported 2D FE and other memory devices regarding W/E ratio, W/E speed, retention, and endurance are shown in **Supplementary Table 3**. In addition to the three-terminal FET devices, we have tested the cycle life of the ferroelectric vertical two-terminal α-In_2Se_3 devices. As shown in **Supplementary Fig. 36**, the vertical α-In_2Se_3 device is stable over 100 cycles and shows no degradation of HRS and LRS after 500 write and erase cycles.

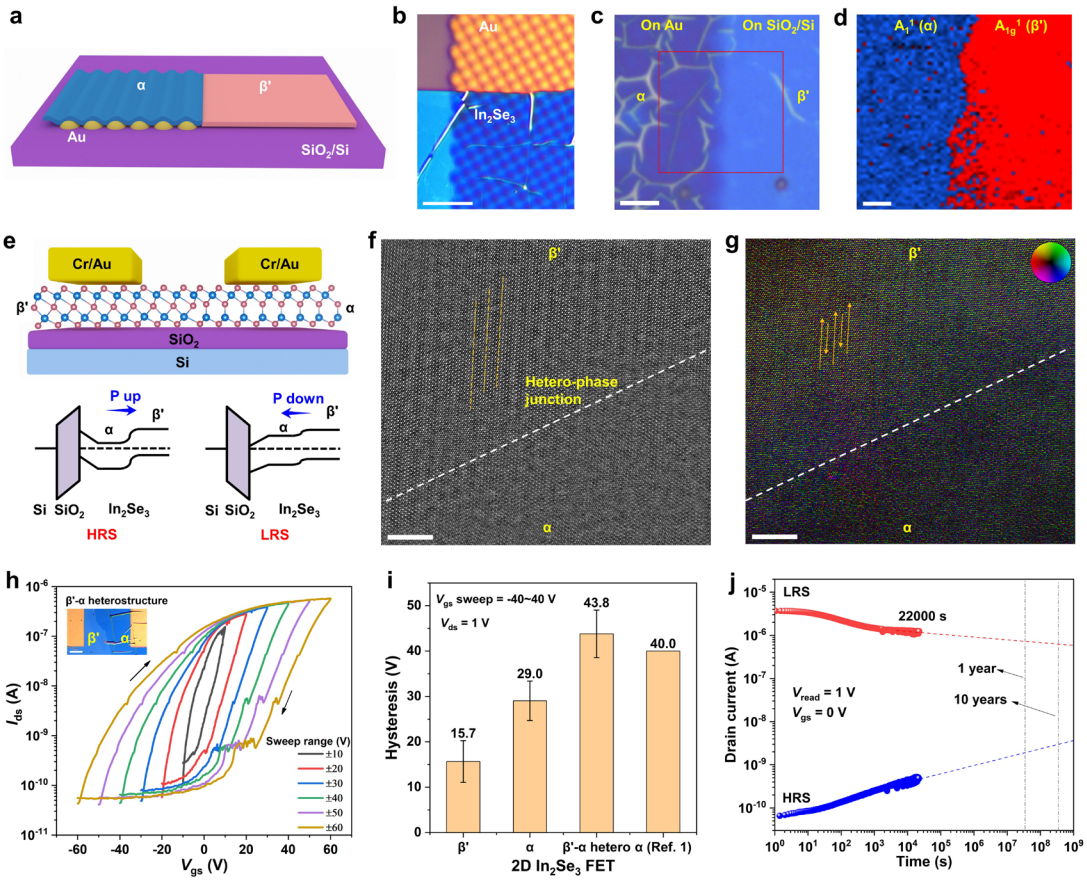

Fig. 4 Fabrication and device application of in-plane α-β′ In_2Se_3 hetero-phase junctions. a, Scheme of the strain-induced fabrication process of α-β′ in-plane hetero-phase junctions by gold (Au) particle array. **b**, Optical image of the transferred In_2Se_3 films on Au-particle array pattern. Scalebar = 10 μm. **c**, Optical image of the junction area. Scalebar = 5 μm. **d**, The corresponding merged Raman mapping collected at α phase A_1^1 and β′ A_{1g}^1 peaks from the red box area in **c**. Scalebar = 2 μm. **e**, Schematic diagram of the FET device (above) and the corresponding band diagram (below) of α-β′ n-n junction under V_{gs}=0 V. **f**, The ADF-STEM image of the α-β′ junction. Scalebar = 5 nm. **g**, The electric field mapping of α-β′ junction collected by DPC-STEM corresponding to **f**. The arrows show the polarization directions. **h**, Hysteresis transfer characteristic loops of α-β′ junction devices during double sweeping with various V_{gs} sweep ranges. Scalebar = 10 μm. **i**, The memory window comparison of our β′-, α- and α-β′ hetero-phase junction devices with the devices results in reference [1]. **j**, NVM retention testing of the α-β′ junction device by gate-voltage control (+80 V write, 0 V read, -80 V erase, and 0 V read).

Following the phase control via strain, we are able to fabricate the α-β′ in-plane hetero-phase junctions (α-β′ junction) by gold (Au) particle array patterning on SiO_2/Si substrates (**Fig. 4a, b**). After transfer onto the Au-particle array pattern, the pristine β′-phase In_2Se_3 film transforms into α-phase in the uneven Au pattern area owing to the release of in-plane strain, while the area on the flat SiO_2/Si substrates remain intact, maintaining the pristine β′ phase. As a result, we can realize the α-β′ junctions by one-step transfer (**Fig. 4c, Supplementary Fig. 37**). The Raman mapping result shows the two-phase merged area is uniform, and the interface is sharp and seamless (**Fig. 4d**). As seen in **Fig. 4c**, some wrinkles appear in the α-phase area, a signature of film delamination and β′-α phase transition. Nevertheless, these wrinkles have negligible negative effects on the electronic device performances. Therefore, the strain-induced phase transition can be used not only for large-area 2D α-In_2Se_3 preparation, but also a strategy for controllable hetero-phase junction, simply by pre-patterning the uneven areas on the substrates.

As a junction interfacing two phases, the α-β′ junction benefits from both the band alignment in conventional semiconductor heterojunctions, and the degree of freedom in polarization control under external electric fields. As shown in **Fig. 4e**, the band diagram of α-β′ junction forms type-II band alignment according to the reported electronic structures of α and β′ phases. [44-47] The working mechanism is based on the on-off switch similar to single-phase FETs. When positive V_{gs} is applied, the off state shown in **Fig. 3b** is further strengthened by the increased height of built-in potential barrier at the α-β′ junction, resulting in the high resistance state (HRS). Instead, when the negative V_{gs} is applied, the on state in **Fig. 3a** relates to a reduced height of built-in potential barrier at the α-β′ junction, leading to the low resistance state (LRS). Therefore, the performance of α-β′ junction devices is even higher than that of single-phase devices, as the junction structure magnifies the polarization switch effect, leading to more stable and more distinguishable memory effects.

The atomic structure of α-β′ junction by STEM is shown **Fig. 4f**, revealing an interface region connected by β′ phase with periodic stripes and α phase without stripes. We use differential phase contrast (DPC) STEM to measure the built-in electric field and polarization mapping in the corresponding α-β′ area, as shown in **Fig. 4g**. The overall

electric field is directed from α to β′ phase according to our results, almost perpendicular to the interface. The electrical field is markedly higher in the β′ phase, due to the in-plane polarizations. In addition, β′ phase has lower carrier density, hence weaker electric field screening. The electric field directions in the β′ phase side are marked by the arrows, which is consistent with the antiparallel polarization directions of $[11\bar{2}0]$ in β′ phase. Stronger electric fields are found in opposite directions to the α-β′ interface in the domains of β′ phase, in line with the built-in potentials of α-β′ hetero-phase junction (**Fig. 3e**). This polarizable built-in potential field at the α-β′ hetero-phase junction can provide more profound hysteresis memory effect in devices.

The optical image of one α-β′ junction device (inset of **Fig. 4h**) and the corresponding merged Raman mapping (**Supplementary Fig. 38**) confirm the sharp α-β′ interface. **Fig. 4h** illustrates the hysteresis transfer characteristic loops of α-β′ junction devices with various gate-voltage sweep ranges, and the hysteresis memory windows gradually increase with the gate-voltage sweep range. From the loop under -60 to 60 V, we find the theoretical LRS/HRS ratio of this device (at V_{gs} = 0 V) is over 10^3. After extracting the memory windows, we compare it with the memory windows of the single-phase devices in this work as well as the device performances in literature (**Fig. 4i**). It shows that the α-β′ junctions possess the largest memory window of 43.8 V under -40 to 40 V sweeping. The larger hysteresis window in α-β′ junction devices than that of single-phase devices is enabled by the polarizable hetero-phase junction as we discussed. Moreover, **Fig. 4j** and **Supplementary Fig. 39** demonstrate the NVM retention test of α-β′ junction device by gate-voltage control, which show a long retention time over 22000 s and remarkable endurance for 6000 cycles. After 22000 s continuous work, the device can still maintain a stable LRS and HRS. We also compared three different hetero-phase-junction memory transistors as summarized in **Supplementary Fig. 40**. Furthermore, the in-plane rectification effect of α-β′ junction with on/off ratio over 1000 can provide an additional degree of freedom to control the NVM device performance, as shown in **Supplementary Fig. 41**. Therefore, the high carrier mobility and robust non-volatile memory capability in such 2D FE hetero-phase junctions will open new pathways to future logic-in-memory devices.

For wafer-scale devices, we have fabricated a memory device array based on cm-scale β′-In_2Se_3 films for pattern memorization, as shown in **Supplementary Fig. 42a**.

Supplementary Fig. 42b shows the bias-dependent retention measurement of HRS and LRS in a single NVM device reading at V_g=0 V, which reveals the readout current can change in a large range. The 4×4 memory array can realize a multipattern comprising "P", "O", "L", and "Y", as shown in the memorization heatmaps in **Supplementary Fig. 42c**. Our approach for large-area In_2Se_3 films shows a great potential in wafer-scale memory devices.

Conclusions

We have unveiled the phase-controllable synthesis of cm-scale 2D β-, β′-, and α-In_2Se_3 films. The phase-controllable synthesis approaches can be fully rationalized based on the defect and strain effects. Using DFT calculations and *in situ* TEM experiments, we confirm that the Se-deficiency triggers the β→β′ phase transition, which well explains the seeding effect of InSe additive in CVD precursors for the β′ phase growth. Meanwhile, the mechanism of β′→α phase transition by strain relaxation is also validated by our *in situ* Raman spectroscopy experiments and DFT calculations. The memory transistor devices using the 2D β′- and α-In_2Se_3 films exhibit high electron mobility, long retention time, and stable cycle endurance. Furthermore, guided by the uncovered strain relaxation approach, we constructed novel β′-α 2D lateral hetero-phase junctions, with even wider hysteresis windows and greater non-volatile memory properties than the single-phase devices. Considering the correlated phases and FE properties of 2D In_2Se_3, and the polarizable hetero-phase junction realized, our phase-controllable synthetic strategies of large-area 2D In_2Se_3 films can open numerous opportunities in developing novel structures and concepts for future FE electronics as well as logic-in-memory devices.

Methods

The In_2Se_3 films were grown by CVD in a two-zone tube furnace (LFT1200C, CPI). The length of quartz tube is 100 cm, and its inner diameter is about 2.5 cm. The high-purity 5% H_2/N_2 mixed gas and argon were used for the CVD process. The gas-flow rate is controlled by a gas flowmeter (Cole-Parmer) with precision of 0.1 standard cubic centimeters per minute (sccm). The exfoliated mica ($KMg_3AlSi_3O_{10}F_2$, Changchun Taiyuan) sheets with size of 1 cm × 1 cm were used for the substrates. An arc quartz boat with size of 10 cm × 1cm × 0.5 cm was used for loading the precursor powders and mica substrates. The Se powder was placed in a ceramic boat. Before heating, the tube is scrubbed by H_2/N_2 mixed gas or argon to remove the oxygen (vacuum for 10 minutes and gas washing for 5 minutes). All the CVD reactions were performed under atmospheric pressure.

Growth of β-In_2Se_3 films. In a typical CVD process, 6 mg of In_2O_3 (99.99%, Alfa) and 3 fresh mica sheets were loaded into the quartz boat and placed in the downstream zone 2 (T_2 = 560-760 °C, heating rate of 20 °C /min). The In_2O_3 powder was evenly dispersed and the mica sheets were placed above the powder with 2 mm distance. 60 mg of Se (99.99%, Innochem) powder was placed in the upstream zone 1 (T_1 = 300 °C, heating rate of 10 °C /min). The H_2/N_2 mixed gas (30 sccm) was used as carrier and reduction gas. The reaction process was kept for 10-30 min. After growth, the furnace was cooled to room temperature naturally.

Growth of β′-In_2Se_3 films. The InSe crystals was synthesized by heating of In_2Se_3 powder (99.99%, Innochem) at 950 °C for 30 min under H_2/N_2 mixed gas (30 sccm). And then the InSe powder was obtained by grinding the InSe crystals. In CVD process, 6 mg of In_2O_3 and InSe mixture (Mass mixing ratio, In_2O_3: InSe = 1:10 or 10:10) was dispersed in the quartz boat and the mica sheets were placed above the powder with 2 mm distance. The boat was placed in the downstream zone 2 (T_2 = 560-660 °C, heating rate of 20 °C /min). 60 mg of Se powder was placed in the upstream zone 1 (T_1 = 300 °C, heating rate of 10 °C /min). The H_2/N_2 mixed gas of 30 sccm was used as carrier and reduction gas. The reaction process was maintained for 10-30 min. After reaction, the furnace was cooled to room temperature naturally.

Transfer method of In_2Se_3 films. The In_2Se_3 films were transferred from mica to TEM grids or other substrates by a poly (methyl methacrylate) (PMMA) method. The PMMA solution was first spin-coated to the mica with 3000 rpm for 60 s, and then heated at

100 °C for 5 min. Secondly, the PMMA was spin-coated again to the mica with 1000 rpm for 60 s and heated at 100 °C for 5 min. After that, the PMMA with In_2Se_3 films was stripped off from the mica by blue tapes in water. Then the PMMA films covered the grids or other substrates and baked at 60 °C for 10 min to remove the water. Finally, the PMMA was removed by immersing in acetone.

Synthesis of α-In_2Se_3 films. The metastable β′-phase In_2Se_3 can be transformed into a more stable α-phase by releasing the strain. We release the strain of β′-phase In_2Se_3 films by transferring them to flexible PET substrates. The process is similar with above transfer method. We removed the PMMA completely by immersing the PET in acetone and dry in vacuum. After that, we bend the PET substrates several times to make the films a complete phase transition. Finally, the large-area α-In_2Se_3 films were obtained.

Materials characterizations. The In_2Se_3 films were characterized by OM (Leica, DM2700M and DM1750M), AFM (Hitachi 5300E), PFM (Asylum Research MFP-3D Infinity and Cypher S), Raman spectroscopy (WITec, Alpha300R, 532 nm laser), SHG (home-built SHG tester using 800 nm laser), XPS (Thermo Fisher Nexsa) and TEM (JEOL, JEM-2100F, acceleration voltage of 200 kV). The XRD patterns of precursors were tested by Rigaku SmartLab 9kW. For *in situ* bending experiments, we used a strain apparatus to load the bending strain. The cross-section TEM samples were prepared by a dual beam FIB/SEM system (FEI Helios G4 UX). The ADF-STEM and DPC-STEM images were collected in an aberration corrected Thermo Fisher Spectra 300 STEM operated at 300 kV. The collection angle of images was 45-200 mrad. The ADF-STEM images were filtered by Wiener filtering to reduce noise. The simulated STEM images were achieved by the software Dr. Probe. [48] The EDS data was collected by Super-X Detector in Thermo Fisher Spectra 300, which was calibrated by standard samples and single-crystal samples (In_2Se_3 and InSe). The solid angle is 0.7 srad and the collecting time is 30 s. The range of deadtime is from 6% to 10%.

***In situ* TEM.** The Protochips Fusion holder and heating E-chips were used for *in situ* heating study in a JEM-2100F TEM at acceleration voltage of 200 kV. The heating E-chips have 9 holes with 7 μm diameter and the silicon nitride films cover the holes. First, the InSe single crystals were ultrasonic dispersed for 30 min and then were dropped onto the holes in E-chip. Next, the E-chip was loaded to the Fusion holder. Before *in situ* experiments, the temperature of E-chip was calibrated. During experiments, the heating and cooling rate was set to 30 °C min^{-1}.

Fabrication of Au particle patterns. We use the Quantifoil TEM grids with pre-defined holes (diameter of 1.2 μm) as hard-mask to deposite Cr/Au metals. Firstly, the grids were pasted onto the SiO_2/Si substrates. And then, 10 nm Cr and 40 nm Au were deposited by an e-beam deposition machine (Denton Explorer E-beam Deposition System). After removing the grids, the Au particle patterns were fabricated.

Device fabrication and characterization. For β and β′-In_2Se_3, the films were transferred to the SiO_2/Si substrates. For α-In_2Se_3, the films were transferred to the Au particle patterns on SiO_2/Si substrates. We use TEM grids without carbon films as hard-mask to define the channels (about 36 or 28 μm length) and source-drain pads (squares with side length of 84 or 55 μm) for back-gate transistors. And then, 10 nm Cr and 50 nm Au were deposited (Denton Explorer E-beam Deposition System). After removing the grids, 10 nm Al_2O_3 layer was deposited by ALD (Ultratech) to encapsulate the devices. The back-gate FETs were tested by the semiconductor analyzer (Keithley 4200) in a probe station (Lake Shore CRX-6.5K) under vacuum and dark environment.

Extraction of electrical parameters. The field-effect mobility (μ) was computed from the equation $\mu = [dI_{ds}/dV_{gs}] \times [L/(WC_iV_{ds})]$, where dI_{ds}/dV_{gs} is the maximum transconductance; and L and W are the channel length and width, respectively; and C_i is the capacitance of 300 nm thick SiO_2 (1.15×10^{-4} F m^{-2}); and V_{ds} is the drain voltage. The maximum hysteresis window ($V_{hysteresis}$) was calculated from the equation $V_{hysteresis} = V_{reverse} - V_{forward}$, under the same drain current.

DFT calculations. Density functional theory (DFT) calculations were performed using Vienna Ab Initio Simulation Package (VASP.5.4.4.18) with projector augmented wave (PAW) [49] potentials. [50,51] The van der Waals Density Functional (vdW-DF) was adopted to describe dispersed interaction. [52-54] The kinetic energy cutoff was set to 350 eV. We took $3 \times 2\sqrt{3}$ supercell for α and reconstructed β′ phase to avoid periodic imaged interaction between Se vacancies. The Brillouin zone was sampled using Γ-centered $3 \times 3 \times 1$ k-points-grids. Total energy and all forces on atoms were converged to less than 10^{-5} eV and 0.02 eV/Å, respectively. The vacuum space of more than 15 Å along the z direction was used to minimize artificial periodic interactions.

Data availability. All relevant data are either supplied in the paper and Supplementary Information, or available from the author upon request.

Code availability. All relevant codes are either provided in the paper or available from the author upon request.

References

1. Si, M. et al. A ferroelectric semiconductor field-effect transistor. *Nat. Electron.* **2**, 580–586 (2019).

2. Wu, J. B. et al. High tunnelling electroresistance in a ferroelectric van der Waals heterojunction via giant barrier height modulation. *Nat. Electron.* **3**, 466–472 (2020).

3. Wang, S. et al. Two-dimensional ferroelectric channel transistors integrating ultra-fast memory and neural computing. *Nat. Commun.* **12**, 53 (2021).

4. Wang, X. W. et al. Van der Waals engineering of ferroelectric heterostructures for long-retention memory. *Nat. Commun.* **12**, 1109 (2021).

5. Dai, M. et al. Two-Dimensional van der Waals Materials with Aligned In-Plane Polarization and Large Piezoelectric Effect for Self-Powered Piezoelectric Sensors. *Nano Lett.* **19**, 5410-5416 (2019).

6. Marega, G. M. et al. Logic-in-memory based on an atomically thin semiconductor. *Nature* **587**, 72–77 (2020).

7. Ielmini, D. & Wong, H.-S. P. In-memory computing with resistive switching devices. *Nat. Electron.* **1**, 333–343 (2018).

8. Khan, A.I. et al. The future of ferroelectric field-effect transistor technology. *Nat. Electron.* **3**, 588–597 (2020).

9. Tong, L. et al. 2D materials–based homogeneous transistor-memory architecture for neuromorphic hardware. *Science* **373**, 1353–1358 (2021).

10. Ding, W. J. et al. Prediction of intrinsic two-dimensional ferroelectrics in In_2Se_3 and other III2-VI3 van der Waals materials. *Nat. Commun.* **8**, 14956 (2017).

11. Zhou, Y. et al. Out-of-plane piezoelectricity and ferroelectricity in layered α-In_2Se_3 nanoflakes. *Nano Lett.* **17**, 5508–5513 (2017).

12. Xue, F. et al. Room-temperature ferroelectricity in hexagonally layered α-In_2Se_3 nanoflakes down to the monolayer limit. *Adv. Funct. Mater.* **28**, 1803738 (2018).
13. Cui, C. et al. Intercorrelated In-Plane and Out-of-Plane Ferroelectricity in Ultrathin Two-Dimensional Layered Semiconductor In_2Se_3. *Nano Lett.* **18**, 1253-1258 (2018).
14. Chang, K. et al. Discovery of robust in-plane ferroelectricity in atomic-thick SnTe. *Science* **353**, 274–278 (2016).
15. Liu, F. et al. Room-temperature ferroelectricity in $CuInP_2S_6$ ultrathin flakes. *Nat. Commun.* **7**, 12357 (2016).
16. Yuan, S. et al. Room-temperature ferroelectricity in $MoTe_2$ down to the atomic monolayer limit. *Nat. Commun.* **10**, 1775 (2019).
17. Bao, Y. et al. Gate-tunable in-plane ferroelectricity in few-layer SnS. *Nano letters*, **19**, 5109-5117 (2019).
18. Zheng, C. et al. Room temperature in-plane ferroelectricity in van der Waals In_2Se_3. *Sci. Adv.* **4**, eaar7720 (2018).
19. Xu, C. et al. Two-dimensional antiferroelectricity in nanostripe-ordered In_2Se_3. *Phys. Rev. Lett.* **125**, 047601 (2020).
20. Chen, Z. et al. Atomic Imaging of Electrically Switchable Striped Domains in β′-In_2Se_3. *Adv. Sci.* **8**, 2100713 (2021).
21. Zhang, Z. M. et al. Atomic visualization and switching of ferroelectric order in β-In_2Se_3 films at the single layer limit. *Adv. Mater.* **33**, 202106951 (2021).
22. Xu, C. et al. Two-Dimensional Ferroelasticity in van Der Waals β'-In_2Se_3. *Nat. Commun.* **12**, 3665 (2021).
23. Collins, J. L. et al. Electronic Band Structure of In-Plane Ferroelectric van der Waals β′-In_2Se_3. *ACS Appl. Electron. Mater.* **2**, 213−219 (2020).
24. Han, G. et al. Indium Selenides: Structural Characteristics, Synthesis and Their Thermoelectric Performances. *Small* **10**, 2747-2765 (2014).
25. Tao, X. & Gu, Y. Crystalline−Crystalline Phase Transformation in Two-Dimensional In_2Se_3 Thin Layers. *Nano Lett.* **13**, 3501–3505 (2013).
26. Liu, L. et al. Atomically Resolving Polymorphs and Crystal Structures of In_2Se_3. *Chem. Mater.* **31**, 10143 (2019).

27. Balakrishnan, N. et al. Quantum Confinement and Photoresponsivity of β-In_2Se_3 Nanosheets Grown by Physical Vapour Transport. *2D Mater.* **3**, 025030 (2016).
28. Rashid, R. et al. Shape-control growth of 2D-In_2Se_3 with out-of-plane ferroelectricity by chemical vapor deposition. *Nanoscale* **12**, 20189-20201 (2020).
29. Van Landuyt, J. et al. Phase transitions in In_2Se_3 as studied by electron microscopy and electron diffraction. *Phys. Status Solidi (a)* **3**, 299-314 (1975).
30. Lin, M. et al. Controlled growth of atomically thin In_2Se_3 flakes by van der Waals epitaxy. *J. Am. Chem. Soc.* **135**, 13274-13277 (2013).
31. Balakrishnan, N. et al. Epitaxial growth of-InSe and α, β, and γ-In_2Se_3 on ε-GaSe. *2D Mater.* **5**, 035026 (2018).
32. Li, T. et al. Epitaxial growth of wafer-scale molybdenum disulfide semiconductor single crystals on sapphire. *Nat. Nanotech.* 16, 1201-1207 (2021).
33. Tang, L. et al. Vertical chemical vapor deposition growth of highly uniform 2D transition metal dichalcogenides. *ACS Nano* **4**, 4646–4653 (2020).
34. Lakin, N. M. et al. The identification of In_2O in the gas phase by high resolution electronic spectroscopy. *J. Chem. Phys.* **107**, 4439-4442 (1997).
35. Ly, T. H. et al. Edge delamination of monolayer transition metal dichalcogenides. *ACS Nano* **11**, 7534-7541 (2017).
36. Huang, L. et al. Mechanical origin of martensite-like structures in two-dimensional ReS_2. *Commun. Mater.* **2**, 87 (2021).
37. Vilaplana, R. et al. Experimental and Theoretical Studies on α-In_2Se_3 at High Pressure. *Inorg. Chem.* **57**, 8241−8252 (2018).
38. Li, W., Qian, X., & Li, J. Phase transitions in 2D materials. *Nat. Rev. Mater.* **6**, 829–846 (2021).
39. Yang, S. X. et al Strain engineering of two-dimensional materials: Methods, properties, and applications. *InfoMat* **3**, 397-420 (2021).
40. Zhang, X. et al. Epitaxial growth of few-layer β-In_2Se_3 thin films by metalorganic chemical vapor deposition. *J. Cryst. Growth* **533**, 125471 (2020).
41. Kang, K. et al. High-mobility three-atom-thick semiconducting films with wafer-scale homogeneity. *Nature* **520**, 656–660 (2015).
42. Xu, X. L. et al. Seeded 2D epitaxy of large-area single-crystal films of the van der Waals semiconductor 2H $MoTe_2$. *Science* **372**, 195-200 (2021).

43. Zhou, J. et al. Controlled synthesis of high-quality monolayered α-In_2Se_3 via physical vapor deposition. *Nano Lett.* **15**, 6400-6405 (2015).
44. Zheng, Z. Q. et al. Self-Assembly of the Lateral In_2Se_3/$CuInSe_2$ Heterojunction for Enhanced Photodetection. *ACS Appl. Mater. Interfaces* **9**, 7288−7296 (2017).
45. Yuan, S. G. et al. Enhanced Piezoelectric Response of Layered In_2Se_3/MoS_2 Nanosheet-Based van der Waals Heterostructures. *ACS Appl. Nano Mater.* **3**, 11979−11986 (2020).
46. Collins, J. L. et al. Electronic Band Structure of In-Plane Ferroelectric van der Waals β′-In_2Se_3. *ACS Appl. Electron. Mater.* **2**, 213−219 (2020).
47. Igo, J. et al. Photodefined in-plane heterostructures in two-dimensional In_2Se_3 nanolayers for ultrathin photodiodes. *ACS Appl. Nano Mater.* **2**, 6774-6782 (2019).
48. Barthel, J. Dr. Probe: A software for high-resolution STEM image simulation. *Ultramicroscopy* **193**, 1-11 (2018).
49. Blöchl, P. E. Projector augmented-wave method. *Phys. Rev. B* **50**, 17953-17979 (1994).
50. Kresse, G., & Furthmüller, J. Efficient iterative schemes for ab initio total-energy calculations using a plane-wave basis set. *Phys. Rev. B* **54**, 11169 (1996).
51. Kresse, G., & Furthmüller, J. Efficiency of ab-initio total energy calculations for metals and semiconductors using a plane-wave basis set. *Comput. Mater. Sci.* **6**, 15-50 (1996).
52. Dion, M. et al. Van der Waals density functional for general geometries. *Phys. Rev. Lett.* **92**, 246401 (2004).
53. Román-Pérez, G., & Soler, J. M. Efficient implementation of a van der Waals density functional: application to double-wall carbon nanotubes. *Phys. Rev. Lett.* **103**, 096102 (2009).
54. Klimeš, J., Bowler, D. R., & Michaelides, A. Van der Waals density functionals applied to solids. *Phys. Rev. B* **83**, 195131 (2011).

Acknowledgements

This work was supported by National Natural Science Foundation of China (Grant Nos. 51872248, 51922113, 52173230, 22105162), Hong Kong Research Grant Council Collaborative Research Fund (Project No. C5029-18E), Early Career Scheme (Project No. 25301018), the Hong Kong Research Grant Council General Research Fund (Project Nos. 11300820 and 15302419), the City University of Hong Kong (Project Nos. 9680241 and 9229074), The Hong Kong Polytechnic University (Project Nos. 1-ZVGH, ZVRP, 1-BE47, ZE0C, and ZE2F), the Shenzhen Science, Technology and Innovation Commission (Project No. JCYJ20200109110213442).

Author contributions

J.Z., Y.M. and L.T.H. supervised and led the research project. W.H. carried out the synthesis with C.C.T.'s assistance. W.H. and X.D.Z. carried out the TEM and Raman characterizations with F.Y.Z., Y.C., N.W. and L.W.W.'s assistance. K.Y. and M.Y. carried out the DFT calculations and analysis. W.H. carried out the device fabrication and testing with S.P.L and K.H.L.'s assistance. T.F.Y., F.G., W.F.I., J.H.H. and C.S.L. carried out the AFM and PFM characterizations. Q.W. and M.L. carried out the SHG characterizations. All the authors discussed the results and co-wrote the manuscript.

Competing interests

The authors declare no competing interests.

Additional information

Reprints and permissions information is available at www.nature.com/reprints. Correspondence and requests for materials should be addressed to jiongzhao@polyu.edu.hk.